



Fluid flow in subduction zones: The role of solid rheology and compaction pressure



Cian R. Wilson^{a,*}, Marc Spiegelman^{a,b}, Peter E. van Keken^c, Bradley R. Hacker^d

^a Lamont-Doherty Earth Observatory, Columbia University, Palisades, NY 10964, USA

^b Department of Applied Physics and Applied Mathematics, Columbia University, New York, NY 10027, USA

^c Department of Earth and Environmental Sciences, 1100 North University Avenue, 2534 CC Little Building, University of Michigan, Ann Arbor, MI 48109-1005, USA

^d Earth Science, University of California, Santa Barbara, CA 93106-9630, USA

ARTICLE INFO

Article history:

Received 30 September 2013

Received in revised form 21 April 2014

Accepted 27 May 2014

Available online 27 June 2014

Editor: T. Elliott

Keywords:

subduction
fluid migration
multi-phase modeling
geodynamics

ABSTRACT

Arc volcanoes tend to occur at locations where the slab is at approximately 100 km depth but most models of fluid production from the downgoing slab suggest fluids are released over a wide range of depths. Reconciling the models with the observations suggests that focusing of slab-produced fluids is necessary if flux-melting is a primary mechanism for the production of arc magmas. This paper investigates one possible mechanism for inducing focusing of fluid flow toward the sub-arc mantle. Through a series of simplified models we explore the role of compaction pressure gradients in modifying fluid flow. These gradients are produced by variations in fluid flux interacting with the permeability and viscosity structure of the solid mantle. When these gradients are neglected, high-permeability systems are dominated by buoyancy and fluid flow is primarily vertical. However, when included, compaction pressure terms have three principal effects: (i) enhancement of upslope flow within high-permeability layers in the slab produced by local dehydration reactions, (ii) deflection of fluids along the sloping rheologically strengthening region in the upper thermal boundary layer, and (iii) production of non-linear porosity waves that locally modulate the flow of fluids and can allow significant transient accumulation of fluids. We demonstrate significant localization of fluid flux toward the sub-arc region due to the permeability and solid viscosity structure. We also estimate the amount of melting expected among the different models and show that models with compaction pressure could produce $\sim 10\%$ flux melting, whereas distributed fluid flow produces $\lesssim 1\%$ in most cases.

© 2014 Elsevier B.V. All rights reserved.

1. Introduction

A robust observation of global subduction-zone volcanism is the location of the primary volcanic arc with respect to the intermediate earthquakes in the subducting slab. In nearly all cases, the depth to the earthquakes beneath the arc is $\sim 100 \pm 40$ km (e.g. Gill, 1981; Jarrard, 1986; Tatsumi, 1986; England et al., 2004; Syracuse and Abers, 2006). The most recent compilations show similar distributions in depth and more remarkably show that this depth is nearly independent of most standard subduction parameters. England et al. (2004) suggested that there is a weak negative correlation with subduction rate, but this is less clear from Syracuse and Abers (2006). Both studies show no correlation with the age of the subducting plate. This result is somewhat puzzling given recent thermal modeling of the production of hydrous fluids

in the subducting plate (van Keken et al., 2011), which suggests that fluid generation is sensitive to the thermal structure of the slab, producing fluids over a wide range of depths.

Slab-derived fluids are a critical part of flux melting. The large variability in fluid production combined with the narrow range of volcano locations suggests a strong focusing mechanism that directs fluids and melts to the hot and shallow regions beneath the volcanic arc. This process appears to be insensitive to the details of subduction. Various mechanisms have been proposed to explain this observation including localized dehydration of amphibole (Tatsumi, 1986), pressure-induced melt suction to the arc corner (Spiegelman and McKenzie, 1987), enhanced thermal advection of anhydrous melt (England and Katz, 2010b), localized stability of chlorite in the wedge (Grove et al., 2009; Till et al., 2012), and lateral flow up thermal boundary layers (Cagnioncle et al., 2007). While many of these ideas are qualitatively appealing and may play a role in controlling the location of arc magmatism, to date there has not been a quantitative model of arc magmatism that has

* Corresponding author.

E-mail address: cwilson@ldeo.columbia.edu (C.R. Wilson).

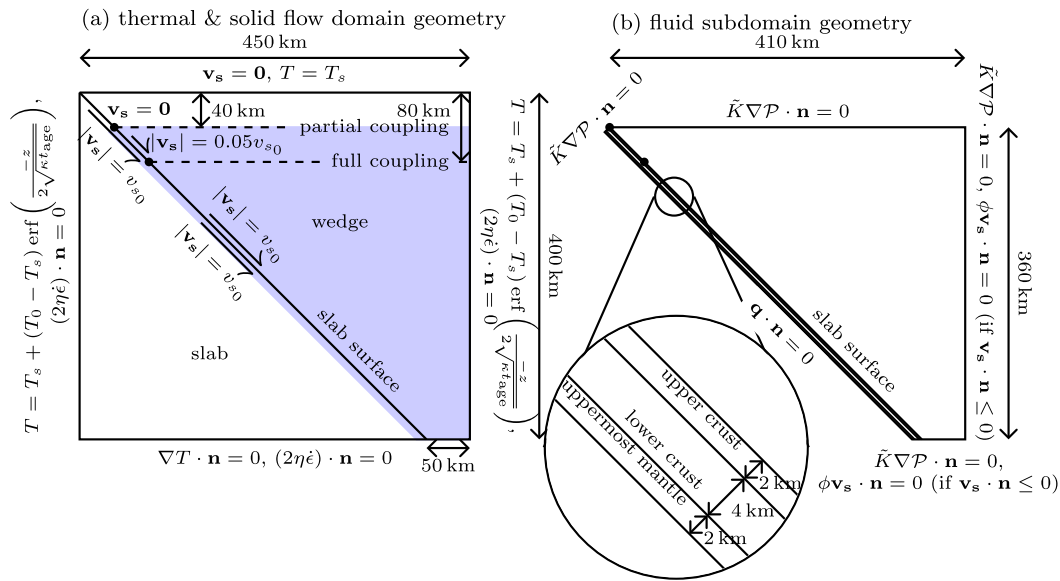


Fig. 1. (a) Geometry layout and boundary conditions for the solid flow calculation. Convergence is forced kinematically along the slab surface. The shaded region represents the subdomain in which fluid flow is calculated. (b) Subdomain geometry and boundary conditions for the fluid-flow calculation corresponding to the region highlighted in (a). $\mathbf{q} \cdot \mathbf{n} = 0$ represents a zero-fluid-flux boundary condition for the compaction pressure, \mathcal{P} , at the base of the subducting slab, where, when non-dimensionalized, $\mathbf{q} = \tilde{K} \nabla \mathcal{P} - K \mathbf{k} - \frac{v_{s0}}{v_{f0}} \phi \mathbf{v}_s$ (6).

been able to produce localized volcanism in the right location. One obvious source of difficulty is that most subduction models either neglect fluid transport or include it in a simple buoyancy-driven approximation (e.g. [Cagnioncle et al., 2007](#); [Wada et al., 2011b](#)) that ignores compaction and fluid–solid interaction.

The purpose of this paper is to develop and explore models that extend recent studies of subduction-zone dynamics and thermal structure ([Syracuse et al., 2010](#); [van Keken et al., 2011](#)) to include a less simplified description of fluid flow. Key features of these models are strongly temperature-dependent rheologies in both slab and wedge, thermodynamically consistent slab-dehydration models and, most importantly, a more physically reasonable model of fluid flow that includes the interaction of fluid transport with the solid rheology. We compare the behavior of these models to simpler models that neglect this interaction, and demonstrate that pressure gradients developed by fluid transport in a spatially variable permeability and rheology structure tend to concentrate fluid flux into the wedge corner.

2. Model

[Fig. 1](#) illustrates the model set up for an idealized geometry with a 45° dipping slab. We determine the solid flow and thermal structure in a manner broadly consistent with [van Keken et al. \(2011\)](#). The fluid migration is then computed without taking the feedback of the fluid on the solid flow into account (as in [Cagnioncle et al., 2007](#); [Wada et al., 2011b](#)).

Two fluid-flow models are considered. The first is the zero-compaction-length approximation ([Spiegelman, 1993a, 1993b](#)), where only the buoyancy and solid velocity affect fluid flow. This model is similar to that of [Cagnioncle et al. \(2007\)](#) except that we include fluid flow in the slab, which contains a thermodynamically consistent water source distributed over a large depth range, rather than a spatially localized, idealized Gaussian pulse. Using the same fluid source, our second model couples the solid rheology and fluid flow by including the compaction pressure gradients induced by variations in fluid flux propagating through a compressible matrix with variable permeability and rheology ([Spiegelman, 1993b](#); [Katz et al., 2007](#)).

2.1. Equations

All the equations are derived and non-dimensionalized in the supplementary material (Section S1.1) as approximations of the general equations for fluid flow in viscously deformable porous media ([McKenzie, 1984](#); [Scott and Stevenson, 1984](#); [Scott and Stevenson, 1986](#); [Bercovici and Ricard, 2003](#); [Simpson et al., 2010a](#); [Simpson et al., 2010b](#)). We summarize the main equations below.

2.1.1. Solid flow

The solid flow and thermal state are found by solving the non-dimensionalized incompressible Stokes and thermal energy equations:

$$-\nabla \cdot (2\eta \dot{\epsilon}) + \nabla p^* = 0 \quad (1)$$

$$\nabla \cdot \mathbf{v}_s = 0 \quad (2)$$

$$\frac{\partial T}{\partial t_s} + \mathbf{v}_s \cdot \nabla T - \frac{1}{\text{Pe}} \nabla^2 T = 0 \quad (3)$$

where \mathbf{v}_s is the velocity of the solid phase, p^* is the dynamic pressure, T is the temperature and t_s is the non-dimensional solid time measure. $\text{Pe} = h v_{s0} / \kappa_0$ is the Péclet number, h is the reference length scale, v_{s0} is the convergence rate and κ_0 is the thermal diffusivity. $\dot{\epsilon} = \frac{1}{2}(\nabla \mathbf{v}_s + \nabla \mathbf{v}_s^T)$ is the strain rate tensor. The non-dimensional solid shear viscosity, η , is temperature dependent:

$$\eta = \left(\frac{\eta_0}{\eta_{\text{diff}}} + \frac{\eta_0}{\eta_{\text{max}}} \right)^{-1}$$

where:

$$\eta_{\text{diff}} = \eta_0 \exp \left[\frac{Q}{RT_0} \left(\frac{T_0}{T_s + (T_0 - T_s)T} - 1 \right) \right]$$

representing diffusion creep of olivine ([Kelemen et al., 2003a](#)), η_{max} is the maximum viscosity cap, η_0 and T_0 are the reference mantle viscosity and temperature respectively. T_s is the surface temperature, Q is the activation energy and R is the gas constant. A full list of solid-flow parameters is presented in [Table 1](#).

Table 1

Significant variables and their values for the idealized solid and thermal flow calculations.

Symbol	Formula	Interpretation	Value
h		reference length scale	1 km
$\frac{Q}{RT_0}$		scaled activation energy (Kelemen et al., 2003a)	20
T_0		reference mantle temperature	1673 K
T_s		surface temperature	273 K
η_0		reference mantle viscosity	1×10^{19} Pa s
η_{\max}		viscosity cap	1×10^{24} Pa s
κ_0		thermal diffusivity	7.272×10^{-7} m ² s ⁻¹
v_{s0}		convergence rate	5 cm yr ⁻¹
Pe	$= \frac{hv_{s0}}{\kappa_0}$	Péclet number	2.1803
t_{age}		overriding plate and slab age	50 Myr
g		acceleration due to gravity	9.81 m s ⁻²

2.1.2. Fluid flow

The thermal state calculated from the solution of (1)–(3) drives the release of fluid from the dehydrating slab into the model domain. This leads to the generation of porosity or fluid volume fraction, ϕ , and compaction pressure, \mathcal{P} , according to the non-dimensionalized equations (Katz et al., 2007):

$$\frac{\partial \phi}{\partial t_f} + \frac{v_{s0}}{v_{f0}} \mathbf{v}_s \cdot \nabla \phi = \frac{h^2}{\delta_0^2} \frac{\mathcal{P}}{\tilde{\zeta}} + \frac{v_{s0}}{v_{f0}} \Gamma \quad (4)$$

$$-\nabla \cdot \tilde{K} \nabla \mathcal{P} + \frac{h^2}{\delta_0^2} \frac{\mathcal{P}}{\tilde{\zeta}} = -\nabla \cdot K \mathbf{k} + \frac{v_{s0}}{v_{f0}} \frac{\Delta \rho \Gamma}{\rho_f}. \quad (5)$$

The fluid velocity, \mathbf{v}_f , has been factored out of (4)–(5), but can be calculated using Darcy's equation for the non-dimensionalized fluid flux:

$$\phi \mathbf{v}_f = \frac{v_{s0}}{v_{f0}} \phi \mathbf{v}_s - \tilde{K} \nabla \mathcal{P} + K \mathbf{k} \quad (6)$$

v_{f0} is the reference fluid velocity scale and t_f is the non-dimensionalized fluid time measure. Γ is the rate of mass transfer from solid to fluid. The densities ρ_f and ρ_s are those of the fluid and solid phases respectively and $\Delta \rho = \rho_s - \rho_f$. \mathbf{k} is the unit vector in the direction opposite to gravity. In order to focus on the effects of compaction pressure, \mathcal{P} , on an otherwise primarily buoyancy driven fluid flow we have dropped the dynamic pressure, p^* , from (5) and (6). The potential contribution of the dynamic pressure has been considered in other studies (e.g. Spiegelman and McKenzie, 1987; Faccenda and Mancktelow, 2010; Faccenda et al., 2012).

The compaction pressure becomes significant when the fluid flux varies on length scales comparable to the compaction length (Spiegelman, 1993b):

$$\delta = \sqrt{\frac{K_0}{\mu_0} \phi^{n-m} \eta} \quad (7)$$

with reference value:

$$\delta_0 = \sqrt{\frac{K_0}{\mu_0} \phi_0^{n-m} \eta_0} \quad (8)$$

where $\frac{K_0}{\mu_0}$ is the ratio of the reference background permeability, K_0 , to the fluid shear viscosity, μ_0 . n and m are the porosity exponents in the non-dimensionalized constitutive relations for the permeability, K , and solid bulk viscosity, ζ , respectively:

$$K = \phi^n \quad \zeta = \eta \phi^{-m}. \quad (9)$$

\tilde{K} and $\tilde{\zeta}$ are regularized versions of the non-dimensionalized permeability and bulk viscosity:

$$\tilde{K} = \tilde{\phi}^n \quad \tilde{\zeta} = \eta \tilde{\phi}^{-m}$$

where:

$$\tilde{\phi} = \phi + \phi_\epsilon$$

that ensure (5) does not become singular in the limit $\phi \rightarrow 0$ given some small $\phi_\epsilon > 0$ (Section 2.3). A full list of fluid-flow parameters is presented in Table 2.

2.1.3. Zero-compaction-length approximation

In the zero-compaction-length approximation (Spiegelman, 1993a, 1993b) the fluid flux driven by compaction pressure gradients (the leading term in (5)) is neglected. In this case, (4) and (5) are combined, eliminating \mathcal{P} :

$$\frac{\partial \phi}{\partial t_f} + \mathbf{v}_\phi \cdot \nabla \phi = \frac{v_{s0}}{v_{f0}} \frac{\rho_s \Gamma}{\rho_f} + \nabla \cdot \kappa_\phi \nabla \phi \quad (10)$$

where:

$$\mathbf{v}_\phi = \frac{v_{s0}}{v_{f0}} \mathbf{v}_s + \frac{\partial K}{\partial \phi} \mathbf{k} \quad (11)$$

is the velocity at which porosity propagates in the zero-compaction length approximation (Spiegelman, 1993a, 1993b). This velocity is different from the fluid flux (6) which becomes:

$$\phi \mathbf{v}_f = \frac{v_{s0}}{v_{f0}} \phi \mathbf{v}_s + K \mathbf{k}. \quad (12)$$

Eq. (10) is a kinematic, non-linear wave equation for the porosity which can admit numerically unresolvable shock waves (Spiegelman, 1993a, 1993b). The final term in (10) contains an additional anisotropic diffusivity, κ_ϕ , added to smooth and resolve the shocks. κ_ϕ is anisotropic with $\kappa_{\phi_{xx}} = 10^{-3}$, $\kappa_{\phi_{zz}} = 10^{-1}$, $\kappa_{\phi_{xz}} = \kappa_{\phi_{zx}} = 0$ so the most diffusion occurs in the direction buoyancy is acting.

2.2. Geometry

We solve (1)–(3) for solid velocity, dynamic pressure, and temperature everywhere in a 450 km \times 400 km two-dimensional domain (Fig. 1(a)). Subduction is forced using a kinematic approach (van Keken et al., 2002; Kelemen et al., 2003a; van Keken et al., 2008; Syracuse et al., 2010) by imposing the convergence velocity on an idealized slab surface dipping at 45° through the domain. The temperature in both the slab and overriding plate is initialized using a conductive cooling model for 50 Myr old oceanic crust. The left and right boundaries maintain this temperature throughout the simulation. All other boundary conditions are described in Fig. 1(a) and in more detail in the supplementary material.

Fluid flow is calculated in a subset of the domain, shaded in Fig. 1(a) and shown in detail in Fig. 1(b). This subdomain incorporates the majority of the wedge side of the domain plus an 8 km thick layer beneath the slab surface. The top boundary of the fluid subdomain lies at a depth of 40 km, where we allow free vertical advection of the porosity by the solid velocity and buoyancy. No flux is allowed through the boundary beneath the slab. All other boundary conditions are described in Fig. 1(b) and in the supplementary material.

The domain is meshed using unstructured triangles with an average vertex spacing of 2 km throughout the majority of the fluid subdomain (wherever fluid is potentially released). Away from these regions the resolution drops smoothly to 20 km (Fig. 2(b)). The slab is triangulated using a structured mesh with a resolution of 500 m perpendicular to the slab.

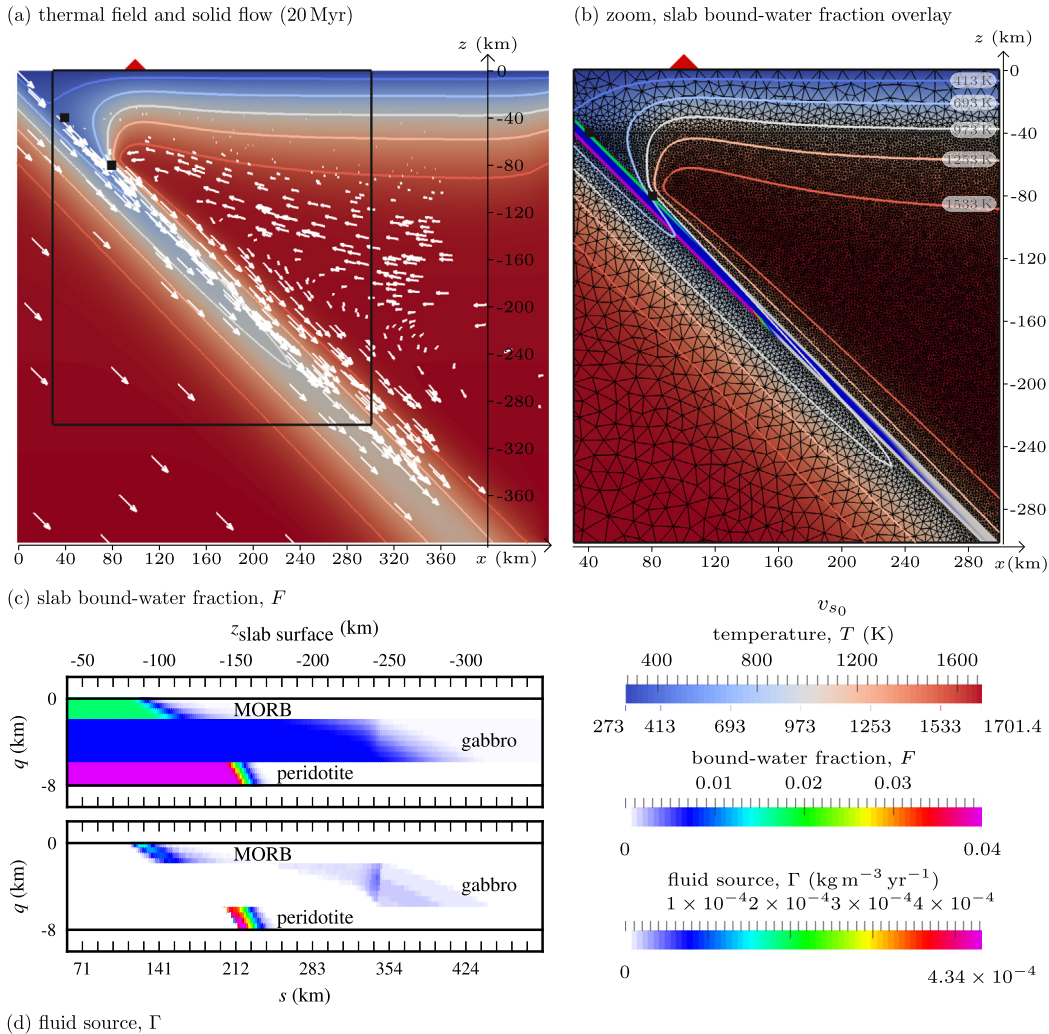


Fig. 2. (a) Solution to (1)–(3) after 20 Myr. The whole $450 \text{ km} \times 400 \text{ km}$ domain is shown. The location of an idealized volcano 100 km above the downgoing slab is indicated by a red triangle. The solid velocity, \mathbf{v}_s , is shown by white glyphs. (b) Close up of the $270 \text{ km} \times 300 \text{ km}$ region highlighted by the black rectangle in (a) showing the high resolution mesh in this area. Both (a) and (b) show the temperature, T , in the background and at labeled contours. The upper and lower black points show the locations of the partial and full coupling points at 40 km and 80 km depth on the slab surface. In (b) the slab is overlain by the slab bound-water fraction, F , given by the phase diagrams in supplementary Figure S1. (c) shows the same bound-water fraction, F , in a reference frame along and perpendicular to the slab, s and q . Decreases in the bound-water fraction along slab, s , correspond to fluid sources, Γ (d). (For interpretation of the references to color in this figure legend, the reader is referred to the web version of this article.)

Within the slab we define three layers; the upper crust (MORB, 2 km thick), lower crust (gabbro, 4 km thick) and uppermost mantle (depleted peridotite, 2 km thick, Fig. 1(b)). To calculate the bound-water fraction in each layer, F , we use tabulated phase diagrams calculated using *Perple_X* (Connolly, 2009) and described by Hacker (2008). Following van Keken et al. (2011), the maximum bound-water content in each lithology is clipped by a lithology-dependent cap, F_{max} ($F_{\text{maxuc}} = 0.02$ in the upper crust, $F_{\text{maxlc}} = 0.007$ in the lower crust and $F_{\text{maxum}} = 0.04$ in the uppermost mantle, see Table 2 and supplementary Figure S1). The non-dimensionalized fluid source, Γ , can then be defined as:

$$\Gamma = -\frac{\mathbf{v}_s \cdot \nabla F}{\phi_0} \quad (13)$$

where ϕ_0 is the reference porosity scale.

2.3. Key parameters

As demonstrated by Cagnioncle et al. (2007), numerous physical parameters affect fluid migration within a subduction zone. In the majority of this study we keep many of these constant (Tables 1 and 2 and supplementary material, Section S1.1) to focus on

the effects of varying the reference permeability-to-fluid viscosity ratio, $\frac{K_0}{\mu_0}$. Scaling arguments can be used to relate this parameter to others in (4)–(5) and (10).

Regardless of the background permeability, the magnitude of fluid flux out of a source area at steady-state must balance the integrated production within it. We can use this to estimate a reference flux and porosity. For example, the fluid flux produced by dehydration of the uppermost mantle layer is roughly:

$$\phi_0 v_{f_0} = \frac{\rho_s v_{s_0} F_{\text{maxum}} d_s}{\rho_f l_s} \approx \frac{\rho_s v_{s_0} F_{\text{maxum}}}{\rho_f} \quad (14)$$

where we have assumed that the length, l_s , over which the slab dehydrates is approximately equal to the depth extent of the source, d_s (see Table 2 for an explanation of the other parameters). Similarly, at reference values, Darcy's law gives us:

$$\phi_0 v_{f_0} = \frac{K_0}{\mu_0} \phi_0^n \Delta \rho g. \quad (15)$$

Equating (14) and (15) gives the reference porosity:

Table 2Significant variables and their values for the idealized fluid flow calculations. Unlisted parameters are the same as in [Table 1](#).

Symbol	Formula	Interpretation	Value(s)		
ρ_s		solid density	3300 kg m ⁻³		
ρ_f		fluid density	1000 kg m ⁻³		
$\Delta\rho$	$= \rho_s - \rho_f$	density difference	2300 kg m ⁻³		
n		permeability porosity exponent	2		
m		bulk viscosity porosity exponent	1		
η_{\max}		viscosity cap (in bulk viscosity)	10 ²¹ Pa s		
$F_{\max_{uc}}$		upper crust max bound-water fraction	0.02		
$F_{\max_{lc}}$		lower crust max bound-water fraction	0.007		
$F_{\max_{um}}$		uppermost mantle max bound-water fraction	0.04		
δ_ϵ		minimum compaction length	1 km		
$K_{\phi_{xx}}$		horizontal porosity diffusion stabilization	10 ⁻³		
$K_{\phi_{zz}}$		vertical porosity diffusion stabilization	10 ⁻¹		
		<i>fluid mobility</i>	'low'	'moderate'	'high'
$\frac{K_0}{\mu_0}$		reference permeability-to-fluid viscosity ratio	1.33 × 10 ⁻¹¹	1.33 × 10 ⁻⁹	1.33 × 10 ⁻⁷ m ³ s kg ⁻¹
ϕ_0	$= \left(\frac{\rho_s F_{\max_{um}} v_{s0}}{\rho_f \frac{K_0}{\mu_0} g \Delta\rho} \right)^{\frac{1}{n}}$ (16)	reference porosity	0.0264	0.00264	0.000264
v_{f0}	$= \frac{K_0}{\mu_0} \phi_0^{n-1} \Delta\rho g$ (17)	reference fluid velocity	0.25	2.5	25 myr ⁻¹
$\frac{v_{f0}}{v_{s0}}$	$= \frac{K_0}{\mu_0} \phi_0^{n-1} \Delta\rho g$ (18)	reference fluid-to-solid velocity ratio	5	50	500
t_{f0}	$= \frac{h}{v_{f0}}$	fluid time scale	4000	400	40 yr
δ_0	$= \sqrt{\frac{K_0}{\mu_0} \phi_0^{n-m} \eta_0}$ (8)	reference compaction length	1.87	5.93	18.7 km
ϕ_ϵ	$= \left(\frac{\delta_\epsilon}{\delta_0} \right)^{\frac{2}{n-m}}$ (21)	porosity regularization (non-dimensionalized)	0.2846	0.0285	0.0028

$$\phi_0 = \left(\frac{\rho_s F_{\max_{um}} v_{s0}}{\rho_f \frac{K_0}{\mu_0} \Delta\rho g} \right)^{\frac{1}{n}} \quad (16)$$

and (15) may then be rearranged for the reference fluid velocity:

$$v_{f0} = \frac{K_0}{\mu_0} \phi_0^{n-1} \Delta\rho g. \quad (17)$$

Combining (16) and (17) and dividing by v_{s0} yields the reference fluid-to-solid velocity ratio:

$$\frac{v_{f0}}{v_{s0}} = \left(\frac{\rho_s F_{\max_{um}}}{\rho_f} \right)^{\frac{n-1}{n}} \left(\frac{\Delta\rho g K_0}{v_{s0} \mu_0} \right)^{1/n}, \quad (18)$$

which we refer to as the fluid mobility. At low values of $\frac{v_{f0}}{v_{s0}}$ fluid flow is dominated by solid advection and the fluid phase will be dragged down by the subducting slab and mantle ([Spiegelman and McKenzie, 1987](#); [Cagnioncle et al., 2007](#)). At high values fluid flow is dominated by the pressure gradients acting on it ([Spiegelman and McKenzie, 1987](#)). When only the effects of buoyancy are considered, this results in predominantly vertical fluid flow with only small deviations where the permeability is low ([Cagnioncle et al., 2007](#)). Compaction pressure gradients may act in any direction so, when included, deviations from vertical fluid flow are possible even at high values of $\frac{v_{f0}}{v_{s0}}$.

The largest sources of uncertainty for estimating $\frac{v_{f0}}{v_{s0}}$ in (18) are the parameters $\frac{K_0}{\mu_0}$ and n , which are poorly constrained for hydrous fluids in the mantle. Experimental estimates of permeability-porosity relationships ([Wark and Watson, 1998](#); [Miller et al., 2014](#)) for texturally equilibrated crystalline aggregates show that simple power laws:

$$K = \frac{d^2 \phi^n}{C} \quad (19)$$

provide a reasonable fit for experimentally accessible porosities, $\phi = 0.02$ – 0.2 , where d is the grain size, $C = 50$ – 200 is a geometric term and n is between 2 and 3. For porosities less than 0.02 it is likely that these relationships underestimate the permeabilities as

the theoretical expectation is that networks of tubules should have permeabilities that scale with $n = 2$ (e.g. [Simpson et al., 2010b](#)).

A larger source of uncertainty is the fluid viscosity, μ , which can vary over many orders of magnitude depending on the dissolved silicate content and temperature. [Audétat and Keppler \(2004\)](#) give the approximate relationship:

$$\log_{10} \mu = -4.2 + 0.008c_s \left(\frac{10000}{T^*} - 2 \right) \quad (20)$$

where c_s is the concentration of dissolved silicates (wt%) and T^* is temperature (K). Pure water has a viscosity of order 10^{-4} Pa s that only increases by one order of magnitude for concentrations of 30 wt% silicate. In contrast, basaltic melts have a viscosity ~ 1 – 10 Pa s (comparable to 80 wt% albite-water fluids at 1073 K) and highly silicic melts, e.g. albite with <10 wt% water, can have a viscosity as high as 10^{11} Pa s.

Given this range of viscosities and permeabilities we can place bounds on the possible value of $\frac{v_{f0}}{v_{s0}}$. Using $n = 3$, $C = 200$, $d = 0.5$ mm, $\mu_0 = 10^{-3}$ Pa s, and $v_{s0} = 5$ cm yr⁻¹, (18) yields $\frac{v_{f0}}{v_{s0}} \approx 68$, which is likely to be a significant underestimate of the fluid velocities of primarily aqueous fluids. To explore a wider range of behaviors we fix the parameter $\frac{K_0}{\mu_0}$ so that $\frac{v_{f0}}{v_{s0}}$ has values of 5, 50, and 500. We refer to these cases as low, moderate and high fluid mobility, respectively ([Table 2](#)). The low-mobility case ($\frac{v_{f0}}{v_{s0}} = 5$) is comparable to that used by [Cagnioncle et al. \(2007\)](#), who assumed $\mu_0 = 1$ Pa s. Note also that we use a permeability exponent of $n = 2$ as we expect mean porosities smaller than $\phi = 0.02$.

Two other parameters, the viscosity cap, η_{\max} , and the minimum compaction length, δ_ϵ , directly affect the fluid flow in this study. The viscosity cap is held fixed, $\eta_{\max} = 10^{24}$ Pa s, during the solid and thermal simulations, in which it acts as a cap on the solid shear viscosity. In the fluid simulations it is lowered to 10^{21} Pa s but only affects the simulation through the solid bulk viscosity (9). Reducing the cap on the bulk viscosity mimics the effect of the damage we expect the slab to have undergone during bending and unbending in subduction ([Rose and Korenaga, 2011](#)) and allows the fluid to escape the strong slab. It also places an upper bound on

the compaction length, the length scale over which the compaction pressure affects the fluid flow (7).

The final fluid parameter of interest, $\delta_\epsilon = 1$ km, specifies the lower bound on the compaction length and is selected based on the numerical resolution available (average nodal spacing for compaction pressure ~ 1 km). Given that the smallest shear viscosity in the domain is η_0 , δ_ϵ can be used to determine the non-dimensional regularization porosity, ϕ_ϵ (Table 2):

$$\phi_\epsilon = \left(\frac{\delta_\epsilon}{\delta_0} \right)^{\frac{2}{n-m}} \quad (21)$$

which prevents (5) from becoming singular as $\phi \rightarrow 0$. The effects of varying η_{\max} and δ_ϵ are considered in the supplementary material.

Although not fully coupled to the fluid flow in this study, the thermal and solid state of the subduction zone (1)–(3) affects the fluid by modifying its source distribution, the solid velocity, and, in the cases with compaction pressure, the solid rheology. A key parameter in determining the thermal structure in kinematic models is the assumed coupling depth (Wada and Wang, 2009; Syracuse et al., 2010). This is fixed at 80 km for the majority of our simulations but the effect of varying this parameter on the fluid flux is also considered.

2.4. Numerical methods and software

We discretize three distinct systems of Eqs. (1)–(3), (4)–(5) and (10), using finite elements in space and finite differences in time. Each individual system is non-linear and convergence of the solution within a system is obtained using an iterative Newton solver, which couples all the variables of that system together.

The range of physical behaviors exhibited requires significant variability in discretization strategy (see supplementary material, Section S1.3). To manage this variability we have developed the software package *TerraFERMA*, the Transparent Finite Element Rapid Model Assembler (Wilson et al., submitted for publication), built on the open source libraries FEniCS (Logg, 2011, 2012), PETSc (Balay et al., 2012a, 2012b) and SPuD (Ham et al., 2009). *TerraFERMA* has been successfully tested against numerous geophysical benchmarks (Wilson et al., submitted for publication), including those for subduction (van Keken et al., 2008) and fluid migration (Simpson and Spiegelman, 2011).

3. Results

We begin by briefly discussing the thermal field and solid flow, which are only calculated once before being used as input to multiple fluid-flow calculations. The primary advance in this study is the inclusion of compaction pressure in these simulations, which we compare to models excluding its effects using a variety of fluid sources, mobilities and other parameters.

3.1. Thermal field and solid flow

The temperature is initialized using an error-function solution for half-space cooling of 50 Myr old oceanic crust (side boundary conditions, Fig. 1(a)). As in Syracuse et al. (2010) we find that 20 Myr of evolution allows the slab to reach a near steady state while avoiding excessive diffusive thickening of the overriding plate.

Fig. 2(a) shows the characteristic kinematic corner flow solution for temperature, T , and solid velocity, \mathbf{v}_s , after 20 Myr. Using this thermal structure, the bound-water content, F , is calculated from thermodynamic look-up tables for each slab lithology (Holland and Powell, 2004; Hacker, 2008; Connolly, 2009, see supplementary Fig. S1) and mapped onto the slab in Fig. 2(b).

Given F and \mathbf{v}_s , the fluid source, \mathcal{I} , may be derived using (13). This results in a shallow ($z \sim -80$ km) water source in the upper crust, a deep ($z \sim -240$ km), distributed, low magnitude source in the lower crust and an intermediate depth ($z \sim -150$ km), large magnitude source in the uppermost mantle of the subducting slab (Fig. 2(d)). Here we have assumed uniform hydration of the slab layers. More localized hydration (e.g. along faults, Wada et al., 2012) or later rehydration could affect the distribution of our sources.

3.2. Fluid flow: single source

To assess the effects of multiple, distributed sources of fluid we begin by considering the fluid flow resulting from the dehydration of depleted peridotite in the uppermost mantle layer of the subducting slab (temporarily setting $F_{\max_{uc}} = F_{\max_{lc}} = 0$). This more closely resembles previous studies of fluid migration in subduction zones where typically only a single Gaussian pulse of water was included (Cagnioncle et al., 2007; Wada et al., 2011b).

3.2.1. Zero-compaction-length approximation

Results using the zero-compaction-length approximation, (10) (Spiegelman, 1993a), are presented, time-averaged over 10000 units of non-dimensional time, in Fig. 3(a). One unit of non-dimensional time is an estimate of the time taken for the fluid to move 1 km (see Table 2 for the dimensional time-scales at each mobility). 10000 units was found to be sufficient to minimize the influence of initial, transient effects, that pass within the first ~ 1000 units (see supplementary material).

In the zero-compaction-length approximation, deviations from vertical flow are only caused by advection by the solid velocity field, \mathbf{v}_s (Fig. 2(a)). In Fig. 3(a) this effect can be seen only in regions with low permeability, where a gradual down-dip spreading can be seen directly above the slab with a corresponding arc-ward spreading in the solid counter flow near the top of the domain.

Varying the mobility we distinguish two related trends. First, at low mobility, the solid velocity has a much greater effect on the porosity and larger deviations from vertical flow are visible. At high mobility, no horizontal deviation is noticeable. Second, with increasing mobility there is a decrease in the maximum porosity. The first occurs because changing the mobility changes the relative fluid to solid velocity. In Fig. 3(a) (i) the reference fluid velocity is only five times faster than the solid, resulting in interaction between the phases. In Fig. 3(a) (iii) the reference fluid moves 500 times faster than the solid. Meanwhile, the reduction in porosity with increasing mobility is a straightforward consequence of (14) which states that for constant convergence rate, v_{s0} , and maximum bound-water content, $F_{\max_{um}}$, the flux of fluid produced is constant and independent of permeability. At fixed flux, faster fluid velocities must be compensated by lower porosities.

Despite some horizontal deviations, very little change to the flux distribution occurs. Fluid exits the slab at ~ 150 km depth and travels across the mantle wedge near vertically. No focusing towards the arc takes place and the peak in vertical flux at 40 km depth lies above the 150 km slab surface depth regardless of the fluid mobility (compare Fig. 4(a) (i) to (ii)).

3.2.2. Compaction pressure effects

We now compare the effects of including compaction pressure for the same thermal structure and fluid production rates. Fig. 3(b), shows the porosity, time-averaged over a longer period, $t_f = [0, 20000]$, owing to the slower nature of the initial transient in the presence of compaction pressure (compare supplementary Figs. S2 and S3).

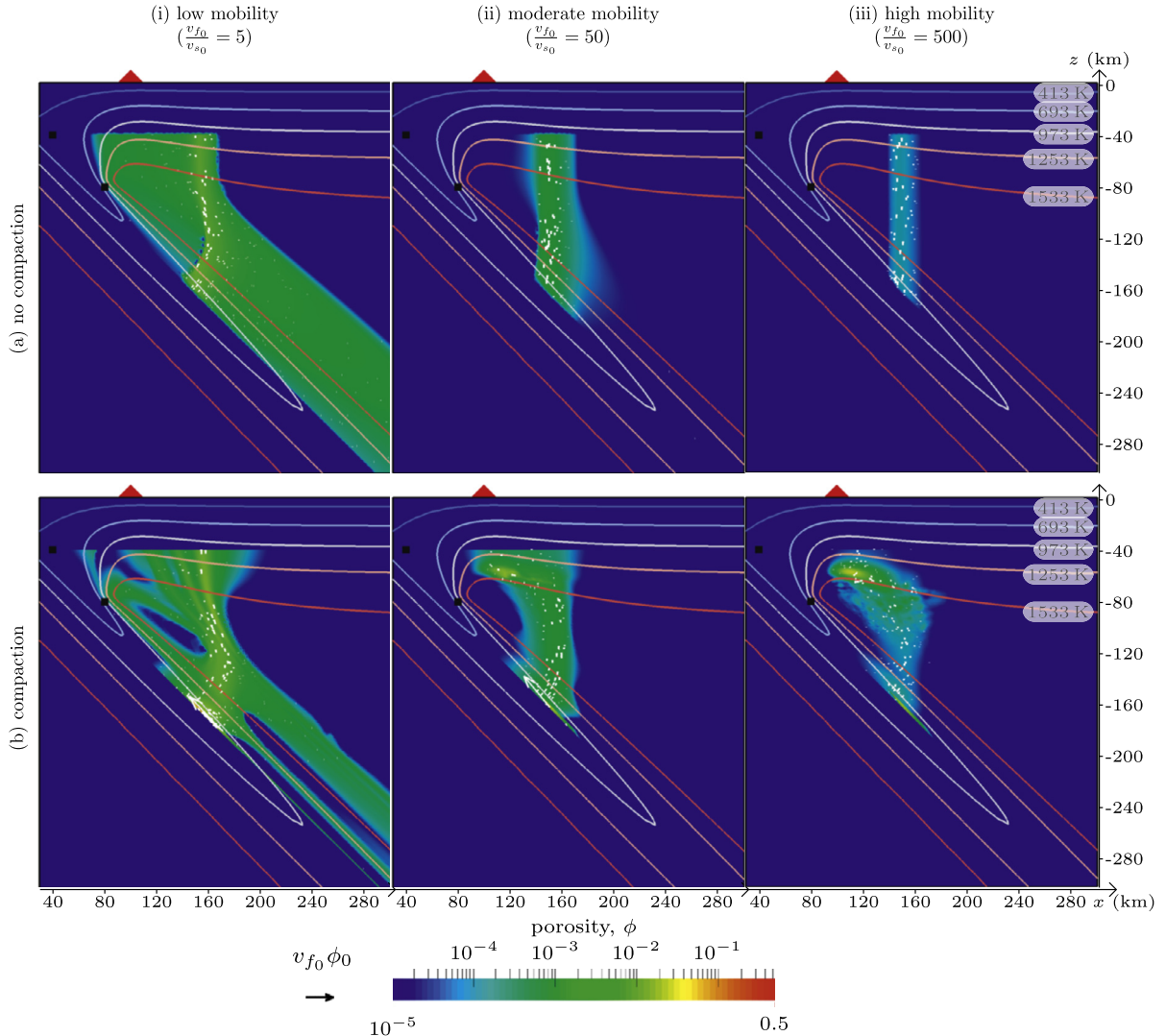


Fig. 3. Time-averaged porosity, ϕ , and fluid flux, ϕv_f (white glyphs, myr^{-1}), from a fluid source in the uppermost mantle (a) excluding and (b) including the effects of compaction pressure at a range of fluid mobilities. Simulations are time-averaged over (a) $t_f = [0, 10\,000]$ and (b) $t_f = [0, 20\,000]$ units of non-dimensional time. Most fluid exits the fluid subdomain (Fig. 1(b)) at 40 km depth. Temperature, T , contours, partial and full coupling points, idealized volcano location and domain shown are the same as in Fig. 2(b). (For interpretation of the references to color in this figure, the reader is referred to the web version of this article.)

Compaction pressure changes the behavior of the fluid flow. Deviations from vertical buoyancy-driven flow are possible anywhere the viscosity or permeability creates an obstacle to the flux (e.g. Spiegelman, 1993a, 1993b). Fluid exits the slab at ~ 150 km depth but once it starts to interact with the colder and stronger overriding plate it gets deflected in a compaction channel and pools beneath the arc. These local accumulations are transient, eventually overcoming the compaction pressure gradient holding them back and exiting the fluid subdomain at 40 km depth (see supplementary Fig. S3(b) (ii, iii)).

Varying the fluid mobility has a more significant effect on the simulation with compaction pressure. At low mobility, the porosity and flux distribution bear similarities to the zero-compaction-length approximation (compare Figs. 3(b) (i) and 3(a) (i)). Increasing the mobility increases the reference compaction length, δ_0 (by increasing $\frac{K_0}{\mu_0}$, see Table 2), extending the distance over which compaction pressure gradients caused by flow toward the strong overriding plate can act. Hence the fluid is deflected arc-ward at greater depth within the mantle wedge (Fig. 3(b) (ii, iii)).

This deflection has a significant effect on the flux compared to the zero-compaction-length case. It substantially modifies the distribution between release from the slab (Fig. 4(b) (ii)) and exit

from the fluid subdomain (Fig. 4(b) (i)). In cases with moderate and high mobility this can be seen to drive the flux toward the shallowest hot and weak region approximately above the 100 km slab surface depth. In the case with low fluid mobility only minor modification in the peak flux occurs between the slab surface and the subdomain top.

3.3. Fluid flow: multiple sources

The hydrated peridotite is the most significant source of fluid in the downgoing slab (Fig. 2(d)) and releases water over a 30 km depth interval. When considering this source of fluid alone, the resulting flux from the slab surface resembles a Gaussian pulse. However, if we consider the full set of fluid sources, the total depth range of fluid release is ~ 230 km from relatively discrete sources in the three layers of the slab (Fig. 2(d)). Reintroducing the upper and lower crustal sources, we now investigate the effects of including a more distributed water source.

3.3.1. Zero-compaction-length approximation

Multiple sources of fluid within the slab do not change the behavior of the zero-compaction-length simulations significantly

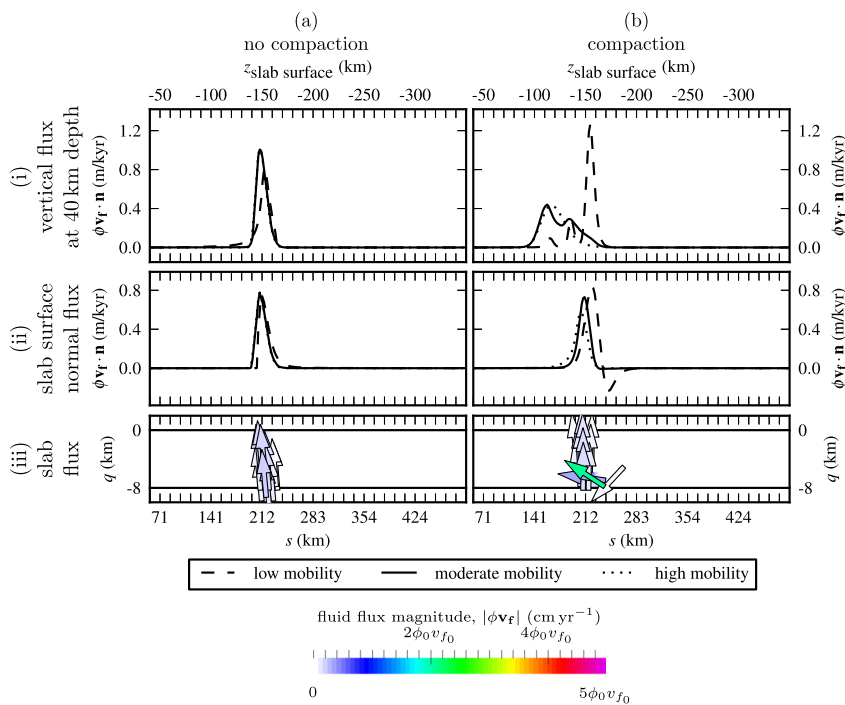


Fig. 4. Time-averaged fluid fluxes from a fluid source in the uppermost mantle (a) excluding and (b) including the effects of compaction pressure. The fluid flux, $\phi \mathbf{v}_f \cdot \mathbf{n}$, (i) normal to the top of the fluid subdomain (at 40 km depth) and (ii) normal to the slab surface are shown at a range of fluid mobilities. For moderate mobility, $\frac{v_{f0}}{v_{s0}} = 50$, a sample of flux vectors with magnitude greater than $0.02\phi_0 v_{f0}$ ($\phi_0 v_{f0} = 6.6 \text{ cm yr}^{-1}$) is shown in a slab coordinate frame (iii). All other parameters are as in Fig. 3. (For interpretation of the references to color in this figure, the reader is referred to the web version of this article.)

(Fig. 5(a)). In the case with low mobility, fluid becomes distributed throughout the mantle wedge, owing to the greater depth distribution of the source. The main flux channel remains evident above the uppermost-mantle source as before. At higher mobilities the flux pathways resolve themselves into distinct plumes from each source with decreasing magnitude of porosity (but increasing fluid velocity).

The flux distribution at the slab surface and at the fluid subdomain top reflect this (Fig. 6(a) (i, ii)), appearing mostly unaltered across the mantle wedge regardless of fluid mobility and showing three distinct peaks in flux corresponding to the slab sources. There is no interaction among the sources in the three layers of the slab (Fig. 6(a) (iii)).

3.3.2. Compaction pressure effects

In the low-mobility case, the inclusion of compaction pressure again has little significant effect on the porosity distribution (compare Figs. 5(a) (i) and 5(b) (i)). The primary flux channel remains apparent above the uppermost-mantle source and no significant deviation of that channel takes place across the mantle wedge although some arc-ward branching of the channel occurs at shallow depths (see Fig. 6(b) (i, ii) dashed line).

With increasing fluid mobility, compaction channels develop beneath the overriding plate as before but significant focusing of the fluid flux also occurs within the slab itself (Figs. 5(b) (ii, iii)). Because the sources of fluids are restricted to thin, dehydrating layers within the downgoing slab, generation of fluid in these layers produces high aspect ratio regions of high porosity aligned with the slab that are overlain by the relatively impermeable mantle wedge. Since compaction pressure gradients redirect fluid through the most permeable regions, the presence of these elongate channels in the slab provide natural pathways to focus the fluid until the fluids can escape into the mantle wedge at shallower depths.

The internal slab fluid flux is shown in a slab reference frame in Fig. 6(b) (iii), demonstrating the connected uppermost-mantle and upper-crustal fluid sources. The weaker lower-crustal source is still disconnected at this moderate mobility. This connectivity contrasts with the weak, disconnected fluxes when compaction pressure is excluded (Fig. 6(a) (iii)).

The increasing connectivity of the fluid from the slab sources with increasing mobility leads to a situation where practically all the fluid flux exits the slab near the location of the shallowest upper-crustal source ($z \sim -80 \text{ km}$, Fig. 6(b) (ii)). Fluids released from this point are redirected back towards the arc, guided by the rheological structure imposed by the temperature field. Eventually, these fluids pond in the shallowest hot and weak zone, approximately above the 100 km slab surface depth (Fig. 6(b) (i)).

3.3.3. Coupling depth

Compaction pressure focuses fluid (i) to the hot, weak corner of the mantle wedge through compaction channels and (ii) to the location of the shallowest fluid source through slab permeability channels. The location of both these sites of focusing is controlled by the full coupling depth in the solid and thermal calculation. The coupling depth sets where the solid mechanically couples with the downgoing slab and so determines how far into the wedge corner hot mantle material is advected. Below the coupling depth the solid wedge flow rapidly heats the slab and so also controls the depth at which the shallowest fluid is released (see supplementary Fig. S1).

We re-evaluate the thermal and solid flow calculations with shallower (60 km) and deeper (100 km) full coupling depths then repeat the fluid flow calculations including all sources and compaction pressure effects. Fig. 7 shows the effect of changing the coupling point depth on both the thermal structure and the fluid focusing. When moved shallower, fluid is released from the slab at approximately 70 km depth (Fig. 7(e) (dashed line)), travels vertically, and leaves the domain above the 70 km slab surface depth

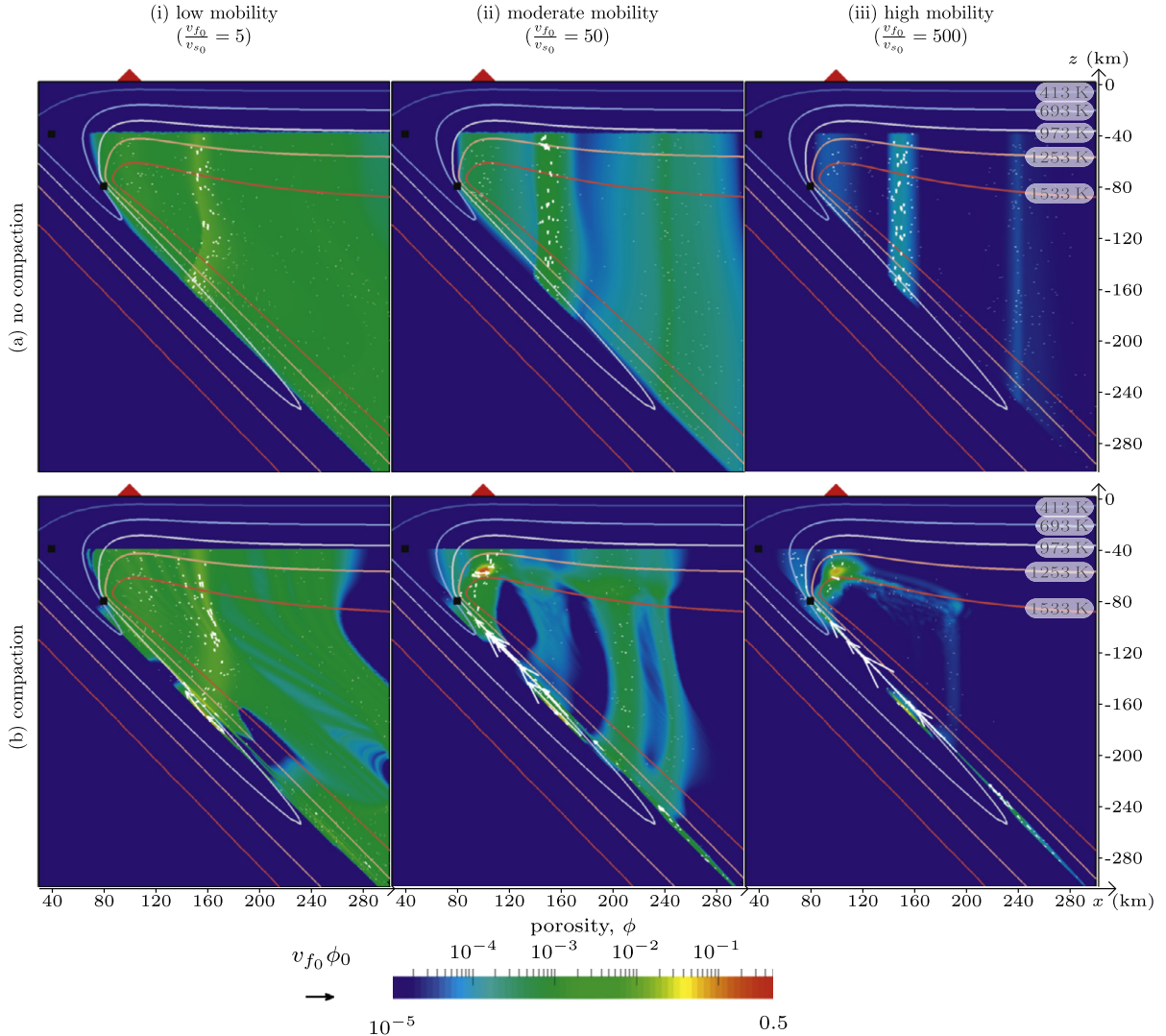


Fig. 5. Time-averaged porosity, ϕ , and fluid flux, $\phi \mathbf{v}_f$ (white glyphs, myr^{-1}), from all sources (a) excluding and (b) including the effects of compaction pressure at a range of fluid mobilities. Simulations are time-averaged over (a) $t_f = [0, 10000]$ and (b) $t_f = [0, 20000]$ units of non-dimensional time. Temperature, T , contours, partial and full coupling points, idealized volcano location and domain shown are the same as in Fig. 2(b). (For interpretation of the references to color in this figure, the reader is referred to the web version of this article.)

(Fig. 7(d) (dashed line)). Moving the coupling point deeper releases fluid at ~ 100 km depth (Fig. 7(e) (dotted line)) from where it ultimately pools and exits the domain above the ~ 120 km slab surface depth (Fig. 7(d) (dotted line)).

4. Discussion

4.1. Fluid focusing

A key requirement of any subduction-zone fluid-migration model is that it reconcile the observation that the depth to earthquakes beneath the arc is $\sim 100 \pm 40$ km (Syracuse and Abers, 2006; England and Katz, 2010a) in spite of the much wider depth distribution of fluid release in the slab (van Keken et al., 2011). The zero-compaction-length approximation, where generally buoyancy is the primary driver of fluid flux, does not provide the necessary focusing.

Introducing a feedback between the solid rheology and the fluid flux through the compaction pressure changes the physics of fluid migration dramatically. Rather than traveling as a non-linear shock front, dispersive porosity waves propagate across the mantle wedge (Spiegelman, 1993b). Most importantly, these waves are de-

flected by variations in permeability and viscosity, changing their size and direction of propagation. This provides two primary fluid-focusing mechanisms in subduction zones.

The first is flow through high-permeability channels formed in the slab around the sites of fluid production. Depending on the background permeability, fluid viscosity, and compaction length scale, these can connect sources that would release fluid at distinct depths along the slab in the zero-compaction-length approximation. Instead, with the introduction of compaction pressure gradients, high fluxes through narrow channels in the layers of the slab itself focus the fluid to shallower depths, typically releasing the bulk of the fluid at the shallowest source near the mechanical coupling point between the slab and wedge.

While the existence and geometry of the high permeability channels is fixed by the slab layering, the focusing mechanism within the channels may depend on the rheology of the slab (Connolly and Podladchikov, 1998). However, any rheological resistance to solid volume changes will produce compaction pressure gradients that drive fluids up the most permeable paths, which suggests that these features should be relatively robust with respect to model assumptions. Direct evidence for the presence of free fluids in the subducting crust below northern Japan is

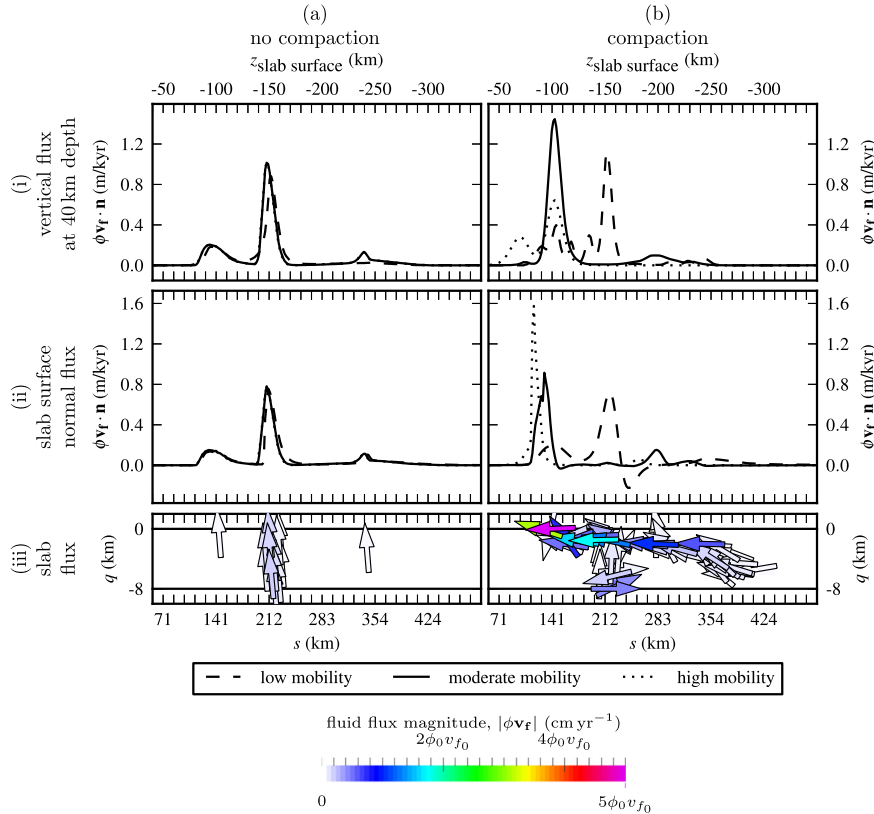


Fig. 6. Time-averaged fluid fluxes from all sources (a) excluding and (b) including the effects of compaction pressure. The fluid flux, $\phi \mathbf{v}_f \cdot \mathbf{n}$, (i) normal to the top of the fluid subdomain (at 40 km depth) and (ii) normal to the slab surface are shown at a range of fluid mobilities. For moderate mobility, $\frac{v_{f0}}{v_{30}} = 50$, a sample of flux vectors with magnitude greater than $0.02\phi_0 v_{f0}$ ($\phi_0 v_{f0} = 6.6 \text{ cm yr}^{-1}$) is shown in a slab coordinate frame (iii). All other parameters are as in Fig. 5. Note that the shallow peak in flux in the high-mobility simulation (b) (i) (dotted line) corresponds to an initial transient. (For interpretation of the references to color in this figure, the reader is referred to the web version of this article.)

provided by Shiina et al. (2013) based on anomalously slow P wavespeeds.

The second focusing mechanism occurs due to fluid interaction with the colder and stronger overriding plate. The importance of this interaction was suggested but not modeled by Cagnioncle et al. (2007). As fluid approaches the increased viscosity at the top of the domain it is deflected by compaction pressure gradients arising because of the increased resistance of the solid to volumetric deformation. Deep-sourced fluid plumes are deflected upslope along the rheological contrast and toward the arc, while shallow dewatering moves away from the trench. Both tend to pool in the shallowest hot and weak zone of the mantle wedge, which lies underneath the idealized arc, above the ~ 100 km slab surface depth.

The location of the hot, weak wedge corner is controlled in the thermal and solid-flow model by the depth of full mechanical coupling between the slab and the mantle wedge (Furukawa, 1993; Wada and Wang, 2009; Syracuse et al., 2010; Wada et al., 2011a). This is constrained by observations of heat flow (Springer and Förster, 1998; Hyndman and Peacock, 2003; Tanaka et al., 2004; Currie and Hyndman, 2006) and seismic attenuation (Nakajima and Hasegawa, 2003; Stachnik et al., 2004; Yoshimoto et al., 2006; Rychert et al., 2008) that demonstrate a sharp thermal contrast in the mantle wedge between a cold corner, down to where the slab is at ~ 80 km depth, and the hot mantle wedge below the arc.

At the full coupling depth, the hot mantle wedge comes into contact with the slab, which experiences rapid heating (see supplementary Fig. S1) and dehydration. The coupling point is therefore generally coincident with the shallowest source of fluid in the slab.

Given the dependence of both the locations of the hot, weak corner and the shallowest source on the coupling depth it is not surprising that there is a correlation between it and location of the maximum fluid flux (Fig. 7). However we note that varying the coupling depth between 60 and 100 km still keeps the primary fluid flux within the observed range of 100 ± 40 km.

4.2. Mobility

Varying the mobility changes the relative time scale of fluid to solid flow and hence the fluid transit time across the mantle wedge. Observations of U-series disequilibria in arc lavas (e.g. Condomines et al., 1988; Gill and Williams, 1990; Elliott et al., 1997; Turner et al., 2003; Reubi et al., 2014) provide indirect constraints on this transit time. While inferences of transport times from U-series disequilibria are model dependent (Spiegelman and Elliott, 1993) and the full U-series systematics of arc lavas are not well understood, it is generally thought that the excess of $^{238}\text{U}/^{230}\text{Th}$ activities in many arc lavas represents a late addition of uranium in slab fluids and a transport time comparable or shorter than the half-life of ^{230}Th , 75.2 kyr. Other arcs show secular equilibrium in $^{238}\text{U}/^{230}\text{Th}$, but radiogenic excesses in ^{231}Pa and ^{226}Ra . In general though, slow-percolation at porosities greater than the bulk partition coefficient of the individual nuclides results in negligible U-series disequilibrium in all elements (Spiegelman and Elliott, 1993).

At reference values the vertical transit times over 100 km are 400, 40, and 4 kyr for low, moderate and high mobility respectively (Table 2). Thus it seems likely that fluid moves too slowly in the low-mobility case to be consistent with the U-series observations.

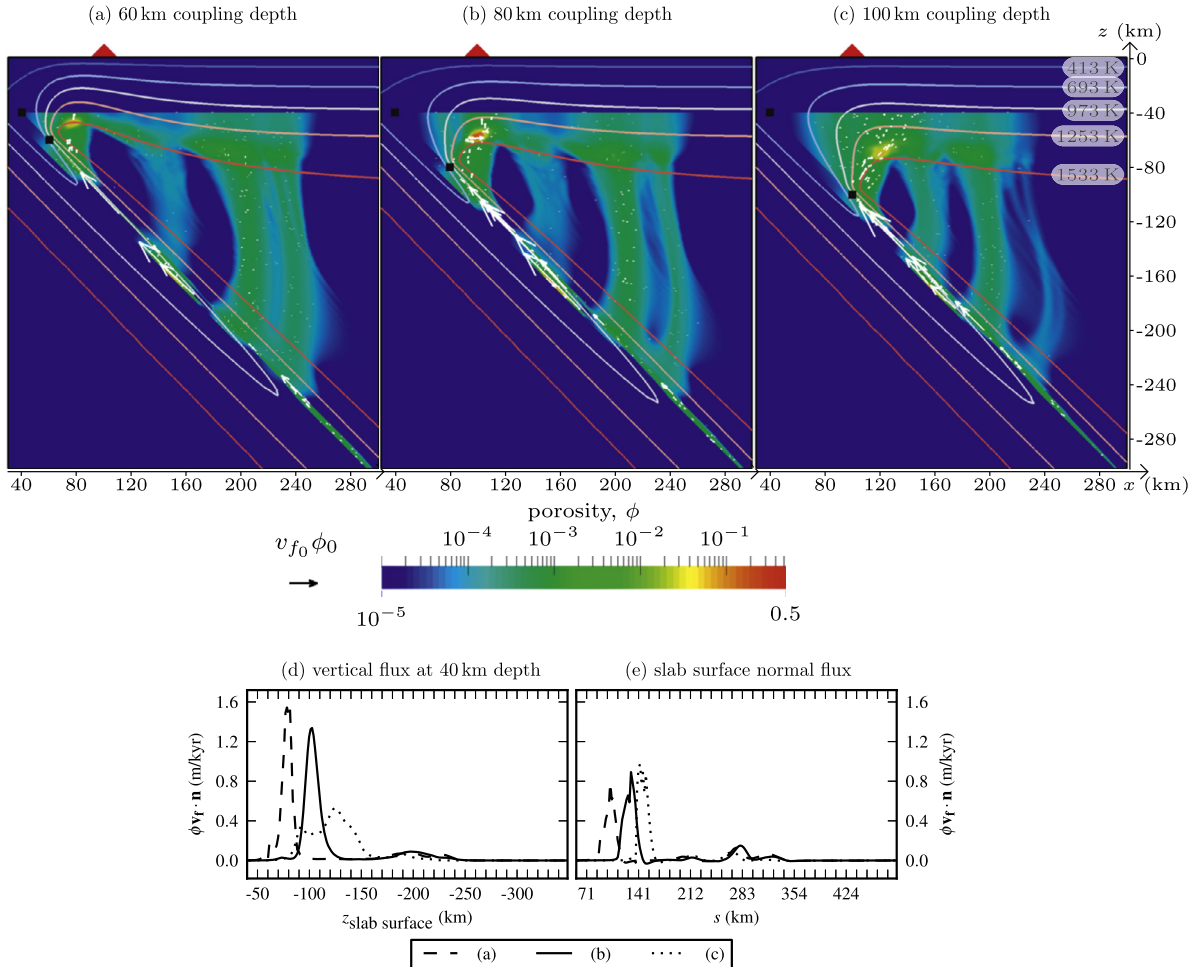


Fig. 7. Simulations including the effects of compaction pressure at a moderate fluid mobility, $\frac{v_{f0}}{v_{s0}} = 50$, varying the full coupling depth in the underlying thermal and solid–flow simulation. Results are time-averaged over $t_f = [0, 20\,000]$ units of non-dimensional time and include all fluid sources. (a)–(c) Porosity, ϕ , and fluid flux, $\phi \mathbf{v}_f$ (white glyphs, m yr^{-1}). (d)–(e) Fluid flux normal, $\phi \mathbf{v}_f \cdot \mathbf{n}$, to (d) the upper boundary of the fluid subdomain (at 40 km depth) and (e) the slab surface for the simulations in (a)–(c). All other annotations are as in Fig. 5. (For interpretation of the references to color in this figure, the reader is referred to the web version of this article.)

4.3. Melting

Another critical observation of global subduction zones is that they produce significant fluxes of high-temperature silicate melts. Dynamical models support the concept that arc volcanism is principally controlled by flux melting, in which the presence of H_2O and other fluxes lower the temperature of the dry solidus (Kelley et al., 2010).

We did not explicitly model the formation of melt, but can use the predictions of fluid migration to estimate the potential for melting in our models. We use the depths, calculated temperatures and time-averaged porosities with the wet-melting parameterization of Kelley et al. (2010) to calculate the potential melt fraction, $F_{\text{melt}} = F_{\text{melt}}(T, z, \phi)$.

In the zero-compaction-length approximation (Fig. 8(a)) a clear inverse correlation exists between fluid mobility and the maximum potential melt fraction, F_{melt} . In the low-mobility case, the maximum melt potential peaks at 11% with a large area of the wedge experiencing at least 1% melting (Fig. 8(a) (i)). As the mobility increases the melt potential decreases as the magnitude of the porosity diminishes (Fig. 8(a) (ii, iii)). In no case is the melt potential concentrated beneath the arc.

When compaction pressure effects are included, no clear correlation exists between fluid mobility and melt fraction, F_{melt} (see Fig. 8(b)). The low-mobility case exhibits behavior similar to the equivalent case excluding compaction pressure. As mobility in-

creases, successive non-linear porosity waves temporarily pool the fluid in the shallow, weak zone of the mantle wedge allowing a higher melt potential in this region than was possible in the zero-compaction-length approximation. In all cases with compaction pressure the melt potential remains above 10%. Due to fluid focusing at moderate and high mobilities the melt is located directly beneath the idealized arc.

The results in Fig. 8 demonstrate that a higher melt fraction is generated when the fluids are focused by compaction pressure. We do note that we did not incorporate the effects of depletion or melt transport here. We also note that the regions of melt potential are colder (1253–1533 K) and at the deep end (~ 60 km) of current estimates for the formation of primitive arc basalts ($\gtrsim 1473$ K, 30–60 km, e.g. Tatsumi et al., 1983; Tanton et al., 2001; Kelemen et al., 2003b; Kelley et al., 2010; Grove et al., 2012), potentially indicating the importance of advective heat transport by fluids and melt (e.g. England and Katz, 2010b).

4.4. Future work

Primarily controlled by convergence rate, slab age and geometry, the global range of subduction zones (England et al., 2004; Syracuse and Abers, 2006) exhibit much wider variability in source distribution (Syracuse et al., 2010; van Keken et al., 2011) than can be approximated in the idealized model used here, where slab age,

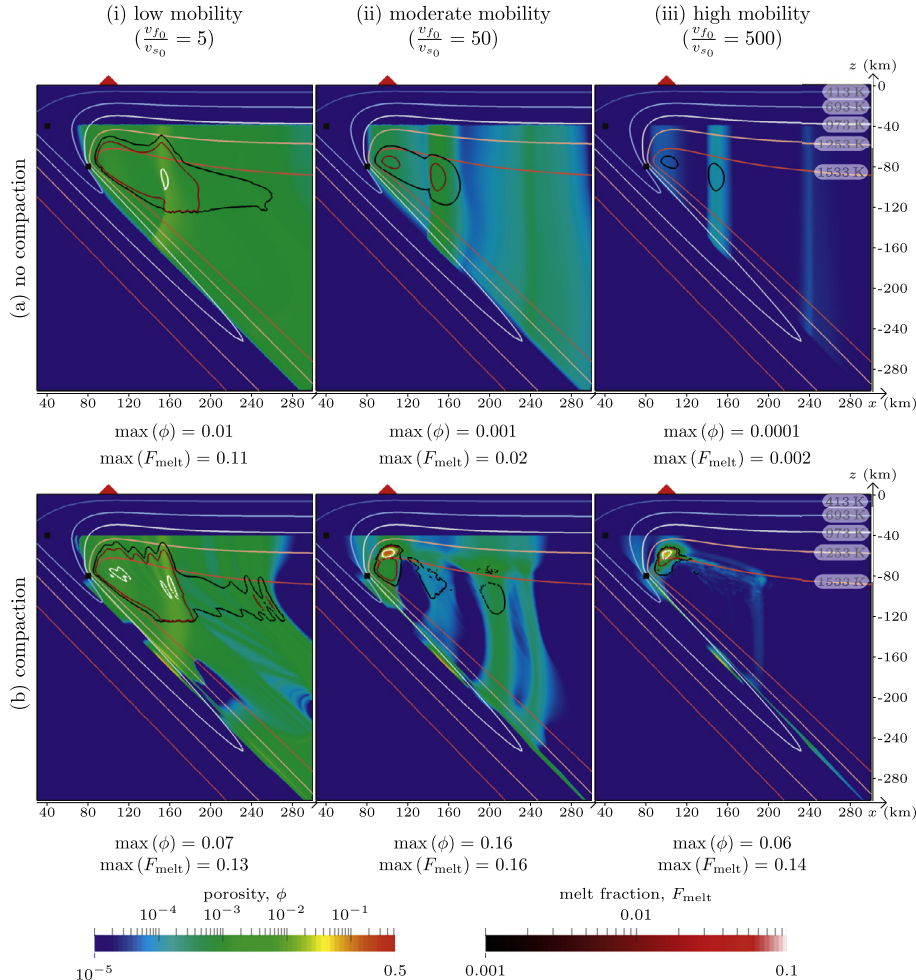


Fig. 8. Porosity, ϕ , and fluid flux, \mathbf{v}_f , as in Fig. 5 overlay with a post-processing calculation of melting potential, F_{melt} , using the parameterization of Kelley et al. (2010). Contours of F_{melt} are shown at values of 0.001 (black), 0.01 (red) and 0.1 (white). The maximum porosity and resulting maximum melt fraction in each time-averaged simulation is also given. The full temperature, $\bar{T} = (T_0 - T_s)T + T_s + T_a \exp(-\text{Di}z) - T_a$, including the adiabat is used in the melt calculation, where $\text{Di} = 2.4525 \times 10^{-4}$ is the Dissipation number and $T_a = 1600$ K is the adiabatic surface temperature. (For interpretation of the references to color in this figure legend, the reader is referred to the web version of this article.)

dip and convergence rate have been held constant. To fully test the efficacy of compaction pressure as a fluid-focusing mechanism, a more comprehensive study across a range of subduction and material parameters is being undertaken to test their effect on fluid migration in these systems. Furthermore, several advances in the model are being implemented to better answer some of the outstanding questions raised here.

Key features that need to be addressed include understanding the effects of potential rehydration reactions on modifying fluid transport (e.g. Wada et al., 2012; Grove et al., 2012), consistent integration of flux melting into the models and potential coupled feedbacks between fluid flow and solid dynamics. Preliminary results on rehydration suggest that rehydration of the cold nose could be significant, providing an effective permeability barrier to further up-dip transport in the slab. In addition, rehydration and weakening of the cold nose by serpentinization is one potential mechanism for mechanically decoupling the slab and mantle wedge, which is currently imposed in the thermal model and of key importance in controlling the fluid flux distribution (e.g. Fig. 7). More generally, weakening of the solid through the introduction of fluid may allow the advection of heat by melt and fluid (Kelemen et al., 2003a; England and Katz, 2010b) to the shallower depths suggested by geochemical and petrological constraints (Tatsumi et al., 1983; Tanton et al., 2001; Kelemen et al., 2003b; Kelley et al., 2010; Grove et al., 2012).

5. Conclusions

The predicted wide distribution of fluid sources in subducting slabs suggests that there must be a robust focusing mechanism acting on fluids that cross the mantle wedge. Buoyancy drives fluids vertically, and only at low permeabilities or high fluid viscosities does interaction with the solid velocity field cause any significant horizontal deviation. At these low fluid velocities the fluid travels slowly enough, hence at sufficient magnitude, to potentially generate melt, but there exists no focusing mechanism to deliver that distributed melt and fluid source to the arc. In addition, these low fluid mobilities are inconsistent with transport rates inferred from uranium series disequilibrium.

If the fluid is allowed to interact not only with the solid velocity but also with the solid rheology, significant focusing of fluid transport paths can take place. This occurs through two primary mechanisms: (i) concentrated fluxes in thin, high-permeability layers in the slab itself and (ii) in compaction channels at the rheological contrast with the base of the overriding plate. Results in an idealized geometry suggest that these mechanisms, induced by the inclusion of compaction pressure, may be a viable method of focusing and concentrating aqueous fluids in subduction zones. The concentration of fluid leaves the potential for melting even at higher, and probably more realistic, permeabilities. Questions remain about the depth and temperature of such melting and also

the effects of feedback from the fluid to the solid through rehydration and rheological weakening.

Acknowledgements

We thank Richard Katz, Ikuko Wada and Tim Elliott for insightful reviews and Mark Behn and other participants at the 4th Computational Infrastructure for Geodynamics workshop on mantle convection and lithosphere dynamics (July 2012, UC Davis, California) for discussions. Supported by National Science Foundation grants OCE-0841079 and EAR-1141976 to CRW and MS, OCE-0841075 to PvK, and EAR-1249703 and EAR-0545441 to BRH.

Appendix A. Supplementary material

Supplementary material related to this article can be found online at <http://dx.doi.org/10.1016/j.epsl.2014.05.052>.

References

- Audéat, A., Keppler, H., 2004. Viscosity of fluids in subduction zones. *Science* 303, 513–516. <http://dx.doi.org/10.1126/science.1092282>.
- Balay, S., Brown, J., Buschelman, K., Eijkhout, V., Gropp, W.D., Kaushik, D., Knepley, M.G., McInnes, L.C., Smith, B.F., Zhang, H., 2012a. PETSc users manual. Technical Report ANL-95/11 - Revision 3.3. Argonne National Laboratory.
- Balay, S., Brown, J., Buschelman, K., Gropp, W.D., Kaushik, D., Knepley, M.G., McInnes, L.C., Smith, B.F., Zhang, H., 2012b. PETSc web page <http://www.mcs.anl.gov/petsc>.
- Bercovici, D., Ricard, Y., 2003. Energetics of a two-phase model of lithospheric damage, shear localization and plate-boundary formation. *Geophys. J. Int.* 152, 581–596. <http://dx.doi.org/10.1046/j.1365-246X.2003.01854.x>.
- Cagnioncle, A.M., Parmentier, E.M., Elkins-Tanton, L.T., 2007. Effect of solid flow above a subducting slab on water distribution and melting at convergent plate boundaries. *J. Geophys. Res.* 112. <http://dx.doi.org/10.1029/2007JB004934>.
- Condomines, M., Hemond, C., Allègre, C., 1988. UThRa radioactive disequilibria and magmatic processes. *Earth Planet. Sci. Lett.* 90, 243–262.
- Connolly, J., 2009. The geodynamic equation of state: what and how. *Geochem. Geophys. Geosyst.* 10. <http://dx.doi.org/10.1029/2009GC002540>.
- Connolly, J., Podladchikov, Y., 1998. Compaction-driven fluid flow in viscoelastic rock. *Geodin. Acta* 11, 55–84. [http://dx.doi.org/10.1016/S0985-3111\(98\)80006-5](http://dx.doi.org/10.1016/S0985-3111(98)80006-5).
- Currie, C.A., Hyndman, R.D., 2006. The thermal structure of subduction zone back arcs. *J. Geophys. Res.* 111, B08404. <http://dx.doi.org/10.1029/2005JB004024>.
- Elliott, T., Plank, T., Zindler, A., White, W., Bourdon, B., 1997. Element transport from slab to volcanic front at the Mariana arc. *J. Geophys. Res., Solid Earth* 102, 14991–15019. <http://dx.doi.org/10.1029/97JB00788>.
- England, P.C., Engdahl, R., Thatcher, W., 2004. Systematic variation in the depths of slabs beneath arc volcanoes. *Geophys. J. Int.* 156, 377–408. <http://dx.doi.org/10.1111/j.1365-246X.2003.02132.x>.
- England, P.C., Katz, R.F., 2010a. Global systematics of arc volcano position. *Nature* 468, E6–E7. <http://dx.doi.org/10.1038/nature09154>.
- England, P.C., Katz, R.F., 2010b. Melting above the anhydrous solidus controls the location of volcanic arcs. *Nature* 467, 700–703. <http://dx.doi.org/10.1038/nature09417>.
- Faccenda, M., Gerya, T.V., Mancktelow, N.S., Moresi, L., 2012. Fluid flow during slab unbending and dehydration: implications for intermediate-depth seismicity, slab weakening and deep water recycling. *Geochem. Geophys. Geosyst.* 13. <http://dx.doi.org/10.1029/2011GC003860>.
- Faccenda, M., Mancktelow, N.S., 2010. Fluid flow during unbending: implications for slab hydration, intermediate-depth earthquakes and deep fluid subduction. *Tectonophysics* 494, 149–154. <http://dx.doi.org/10.1016/j.tecto.2010.08.002>.
- Furukawa, Y., 1993. Depth of decoupling plate interface and thermal structure under arcs. *J. Geophys. Res.* 98, 20005–20013. <http://dx.doi.org/10.1029/93JB02020>.
- Gill, J., Williams, R., 1990. Th isotope and u-series studies of subduction-related volcanic rocks. *Geochim. Cosmochim. Acta* 54, 1427–1442.
- Gill, J.B., 1981. *Orogenic Andesites and Plate Tectonics*. Minerals and Rocks, vol. 16. Springer-Verlag.
- Grove, T.L., Till, C.B., Krawczynski, M.J., 2012. The role of H₂O in subduction zone magmatism. *Annu. Rev. Earth Planet. Sci.* 40, 413–439. <http://dx.doi.org/10.1146/annurev-earth-042711-105310>.
- Grove, T.L., Till, C.B., Lev, E., Chatterjee, N., Médard, E., 2009. Kinematic variables and water transport control the formation and location of arc volcanoes. *Nature* 459, 694–697. <http://dx.doi.org/10.1038/nature08044>.
- Hacker, B.R., 2008. H₂O subduction beyond arcs. *Geochem. Geophys. Geosyst.* 9. <http://dx.doi.org/10.1029/2007GC001707>.
- Ham, D.A., Farrell, P.E., Gorman, G.J., Maddison, J.R., Wilson, C.R., Kramer, S.C., Ship-ton, J., Collins, G.S., Cotter, C.J., Piggott, M.D., 2009. Spud 1.0: generalising and automating the user interfaces of scientific computer models. *Geosci. Model Dev.* 2, 33–42. <http://dx.doi.org/10.5194/gmd-2-33-2009>.
- Holland, T.J.B., Powell, R., 2004. An internally consistent thermodynamic data set for phases of petrological interest. *J. Metamorph. Geol.* 16, 309–343. <http://dx.doi.org/10.1111/j.1525-1314.1998.00140.x>.
- Hyndman, R.D., Peacock, S.M., 2003. Serpentinization of the forearc mantle. *Earth Planet. Sci. Lett.* 212, 417–432. [http://dx.doi.org/10.1016/S0012-821X\(03\)00263-2](http://dx.doi.org/10.1016/S0012-821X(03)00263-2).
- Jarrard, R.D., 1986. Relations among subduction parameters. *Rev. Geophys.* 24, 217. <http://dx.doi.org/10.1029/RG024i002p00217>.
- Katz, R.F., Knepley, M.G., Smith, B., Spiegelman, M., Coon, E.T., 2007. Numerical simulation of geodynamic processes with the portable extensible toolkit for scientific computation. *Phys. Earth Planet. Inter.* 163, 52–68. <http://dx.doi.org/10.1016/j.pepi.2007.04.016>.
- van Keken, P.E., Currie, C., King, S.D., Behn, M.D., Cagnioncle, A.M., He, J.H., Katz, R.F., Lin, S.C., Parmentier, E.M., Spiegelman, M., Wang, K.L., 2008. A community benchmark for subduction zone modeling. *Phys. Earth Planet. Inter.* 171, 187–197. <http://dx.doi.org/10.1016/j.pepi.2008.04.015>.
- van Keken, P.E., Hacker, B.R., Syracuse, E.M., Abers, G.A., 2011. Subduction factory: 4. Depth-dependent flux of H₂O from subducting slabs worldwide. *J. Geophys. Res.* 116. <http://dx.doi.org/10.1029/2010JB007922>.
- van Keken, P.E., Kiefer, B., Peacock, S.M., 2002. High-resolution models of subduction zones: implications for mineral dehydration reactions and the transport of water into the deep mantle. *Geochem. Geophys. Geosyst.* 3, 1056. <http://dx.doi.org/10.1029/2001GC000256>.
- Kelemen, P.B., Rilling, J.L., Parmentier, E.M., Mehl, L., Hacker, B., 2003a. Thermal structure due to solid-state flow in the mantle wedge beneath arcs. *Geophys. Monogr. Ser.* 138, 293–311.
- Kelemen, P.B., Yogodzinski, G.M., Scholl, D.W., 2003b. Along-strike variation in the Aleutian island arc: Genesis of high Mg# andesite and implications for continental crust. In: Eiler, J. (Ed.), *Geophysical Monograph Series*, vol. 138. American Geophysical Union, Washington, DC, pp. 223–276.
- Kelley, K.A., Plank, T., Newman, S., Stolper, E.M., Grove, T.L., Parman, S., Hauri, E.H., 2010. Mantle melting as a function of water content beneath the Mariana arc. *J. Petrol.* <http://dx.doi.org/10.1093/petrology/egq036>.
- Logg, A., 2011. Fenics project. <http://fenicsproject.org>.
- Logg, A., 2012. *Automated Solution of Differential Equations by the Finite Element Method* the FEniCS Book. Springer.
- McKenzie, D., 1984. The generation and compaction of partially molten rock. *J. Petrol.* 25, 713–765. <http://dx.doi.org/10.1093/petrology/25.3.713>.
- Miller, K.J., Zhu, W.L., Montési, L.G.J., Gaetani, G.A., 2014. Experimental quantification of permeability of partially molten mantle rock. *Earth Planet. Sci. Lett.* 388, 273–282. <http://dx.doi.org/10.1016/j.epsl.2013.12.003>.
- Nakajima, J., Hasegawa, A., 2003. Estimation of thermal structure in the mantle wedge of northeastern Japan from seismic attenuation data. *Geophys. Res. Lett.* 30, 1760. <http://dx.doi.org/10.1029/2003GL01785>.
- Reubi, O., Sims, K.W.W., Bourdon, B., 2014. ²³⁸U–²³⁰Th equilibrium in arc magmas and implications for the time scales of mantle metasomatism. *Earth Planet. Sci. Lett.* 391, 146–158. <http://dx.doi.org/10.1016/j.epsl.2014.01.054>.
- Rose, I.R., Korenaga, J., 2011. Mantle rheology and the scaling of bending dissipation in plate tectonics. *J. Geophys. Res.* 116. <http://dx.doi.org/10.1029/2010JB008004>.
- Rychert, C.A., Fischer, K.M., Abers, G.A., Plank, T., Syracuse, E.M., Protti, J.M., Gonzalez, V., Strauch, W., 2008. Strong along-arc variations in the mantle wedge beneath Costa Rica and Nicaragua. *Geochem. Geophys. Geosyst.* 9, Q10S10. <http://dx.doi.org/10.1029/2008GC002040>.
- Scott, D., Stevenson, D., 1984. Magma solitons. *Geophys. Res. Lett.* 11, 1161–1164. <http://dx.doi.org/10.1029/GL011i011p01161>.
- Scott, D., Stevenson, D., 1986. Magma ascent by porous flow. *J. Geophys. Res.* 91, 9283–9296. <http://dx.doi.org/10.1029/JB091iB09p09283>.
- Shiina, T., Nakajima, J., Matsuzawa, T., 2013. Seismic evidence for high pore pressures in the oceanic crust: implications for fluid-related embrittlement. *Geophys. Res. Lett.* 40, 2006–2010. <http://dx.doi.org/10.1002/grl.50468>.
- Simpson, G., Spiegelman, M., 2011. Solitary wave benchmarks in magma dynamics. *J. Sci. Comput.* <http://dx.doi.org/10.1007/s10915-011-9461-y>.
- Simpson, G., Spiegelman, M., Weinstein, M., 2010a. A multiscale model of partial melts: 1. Effective equations. *J. Geophys. Res.* 115. <http://dx.doi.org/10.1029/2009JB006375>.
- Simpson, G., Spiegelman, M., Weinstein, M., 2010b. A multiscale model of partial melts: 2. Numerical results. *J. Geophys. Res.* 115. <http://dx.doi.org/10.1029/2009JB006376>.
- Spiegelman, M., 1993a. Flow in deformable porous media. Part 1 simple analysis. *J. Fluid Mech.* 247, 17–38. <http://dx.doi.org/10.1017/S0022112093000369>.
- Spiegelman, M., 1993b. Flow in deformable porous media. Part 2 numerical analysis – the relationship between shock waves and solitary waves. *J. Fluid Mech.* 247, 39–63. <http://dx.doi.org/10.1017/S0022112093000370>.
- Spiegelman, M., Elliott, T., 1993. Consequences of melt transport for uranium series disequilibrium in young lavas. *Earth Planet. Sci. Lett.* 118, 1–20. [http://dx.doi.org/10.1016/0012-821X\(93\)90155-3](http://dx.doi.org/10.1016/0012-821X(93)90155-3).
- Spiegelman, M., McKenzie, D., 1987. Simple 2-D models for melt extraction at mid-ocean ridges and island arcs. *Earth Planet. Sci. Lett.* 83, 137–152. [http://dx.doi.org/10.1016/0012-821X\(87\)90057-4](http://dx.doi.org/10.1016/0012-821X(87)90057-4).

- Springer, M., Förster, A., 1998. Heat-flow density across the central Andean subduction zone. *Tectonophysics* 291, 123–139.
- Stachnik, J., Abers, G., Christensen, D., 2004. Seismic attenuation and mantle wedge temperatures in the Alaska subduction zone. *J. Geophys. Res.* 109, B10304. <http://dx.doi.org/10.1029/2004JB003018>.
- Syracuse, E.M., Abers, G.A., 2006. Global compilation of variations in slab depth beneath arc volcanoes and implications. *Geochem. Geophys. Geosyst.* 7. <http://dx.doi.org/10.1029/2005GC001045>.
- Syracuse, E.M., van Keken, P.E., Abers, G.A., 2010. The global range of subduction zone thermal models. *Phys. Earth Planet. Inter.* 183, 73–90. <http://dx.doi.org/10.1016/j.pepi.2010.02.004>.
- Tanaka, A., Yamana, M., Yano, Y., Sasada, M., 2004. Geothermal gradient and heat flow data in and around Japan. Digital Geoscience Map DGM P-5.
- Tanton, L.T.E., Grove, T.L., Donnelly-Nolan, J., 2001. Hot, shallow mantle melting under the cascades volcanic arc. *Geology* 29, 631–634.
- Tatsumi, Y., 1986. Formation of the volcanic front in subduction zones. *Geophys. Res. Lett.* 13, 717–720. <http://dx.doi.org/10.1029/GL013i008p00717>.
- Tatsumi, Y., Sakuyama, M., Fukuyama, H., Kushiro, I., 1983. Generation of arc basalt magmas and thermal structure of the mantle wedge in subduction zones. *J. Geophys. Res.* 88, 5815–5825. <http://dx.doi.org/10.1029/JB088iB07p05815>.
- Till, C.B., Grove, T., Withers, A., 2012. The beginnings of hydrous mantle wedge melting. *Contrib. Mineral. Petrol.* 163, 669–688. <http://dx.doi.org/10.1007/s00410-011-0692-6>
- Turner, S., Bourdon, B., Gill, J., 2003. Insights into magma genesis at convergent margins from u-series isotopes. *Rev. Mineral. Geochem.* 52, 255–315. <http://dx.doi.org/10.2113/0520255>.
- Wada, I., Behn, M.D., He, J., 2011a. Grain-size distribution in the mantle wedge of subduction zones. *J. Geophys. Res.* 116, B10203. <http://dx.doi.org/10.1029/2011JB008294>.
- Wada, I., Behn, M.D., Parmentier, E.M., Shaw, A.M., 2011b. Focusing of upward fluid migration due to mineral grain size variation. In: *Goldschmidt Conference, Prague, 2011*.
- Wada, I., Behn, M.D., Shaw, A.M., 2012. Effects of heterogeneous hydration in the incoming plate, slab rehydration, and mantle wedge hydration on slab-derived H₂O flux in subduction zones. *Earth Planet. Sci. Lett.* 353–354, 60–71. <http://dx.doi.org/10.1016/j.epsl.2012.07.025>.
- Wada, I., Wang, K., 2009. Common depth of slab-mantle decoupling: reconciling diversity and uniformity of subduction zones. *Geochem. Geophys. Geosyst.* 10. <http://dx.doi.org/10.1029/2009GC002570>.
- Wark, D.A., Watson, E., 1998. Grain-scale permeabilities of texturally equilibrated, monomineralic rocks. *Earth Planet. Sci. Lett.* 164, 591–605. [http://dx.doi.org/10.1016/S0012-821X\(98\)00252-0](http://dx.doi.org/10.1016/S0012-821X(98)00252-0).
- Wilson, C.R., Spiegelman, M., van Keken, P.E., submitted for publication. TerraFERMA: the transparent finite element rapid model assembler for multiphysics problems in the Earth sciences. *Geochem. Geophys. Geosyst.*
- Yoshimoto, K., Wegler, U., Korn, M., 2006. A volcanic front as a boundary of seismic-attenuation structures in northeastern Honshu, Japan. *Bull. Seismol. Soc. Am.* 96, 637–646. <http://dx.doi.org/10.1785/0120050085>